Journal of Stress Analysis
Vol. 9, No. 1, 2025, 67-80
Bu-Ali Sina University

ORIGINAL RESEARCH PAPER

Stress Analysis in Double-Lap Adhesively Bonded FG Adherend Joints Using FEM and ANN

Nabard Habibi*, **Mazyar Vakil Faraji**
Department of Faculty Engineering, University of Kurdistan, Sanandaj, Iran.

Article info

Article history:
Received 21 March 2025
Received in revised form
06 June 2025
Accepted 25 June 2025

Keywords:
Adhesive bonding
Double-lap
ABAQUSs
FGMs
Stress analysis

Abstract

This study presents a comprehensive numerical investigation of stress distribution in double-lap adhesive joints between functionally graded material (FGM) adherends. Using three-dimensional finite element analysis (FEA) in ABAQUS, this study examined the effects of adhesive thickness, material gradation, and applied load on joint performance. To enhance computational efficiency and predictive capabilities, a feedforward artificial neural network (ANN) model was also developed and trained using simulation data. The results show that adhesive thickness has a significant influence on peak shear stress, with an optimal thickness of 0.2mm minimizing stress concentrations under both 10kN and 50kN tensile loads. The inclusion of FGMs in the adherends improved stress distribution due to the gradual transition in material properties from ceramic to metal. The ANN model, trained on FEA outputs, achieved a high correlation (R^2>0.99) and minimal error (MSE<0.001), validating its capability to provide rapid and accurate stress prediction. The proposed hybrid FEA-ANN framework provides a reliable and efficient tool for designing adhesive joints with graded materials. This approach can be extended to optimize joint configurations in aerospace, automotive, and structural applications where weight and stress management are critical.

1. Introduction

Adhesive joints have been extensively studied due to their ability to distribute stresses efficiently and provide lightweight bonding solutions for aerospace, automotive, and marine structures. General reviews by Ramalho et al. [1] and Akhavan-Safar et al. [2] summarize adhesive joint configurations and bi-adhesive concepts, while Durodola [3] extended the discussion to functionally graded adhesives. Classical analytical foundations remain relevant, with da Silva et al. [4,5] compiling the Volkersen and Goland–Reissner models into benchmark surveys. Experimental and numerical investigations by Carbas et al. [6] and Pires et al. [7] highlighted the role of adhesive type and thickness, while Kong et al. [8] conducted three-dimensional (3D) FEA to capture stress distributions in bi-adhesive joints. Together, these works provide the baseline for later developments in adhesive joint analysis.

Functionally graded adhesives and adherends have gained increasing attention as solutions to mitigate stress concentrations. Jia et al. [9] demonstrated strength enhancement with graphene-reinforced FG adhesives, while Khan et al. [10] used stochastic modeling of double-lap FGM joints. Reviews by Durodola [3] further highlight the potential of FG adhesives in structural applications. Practical advances were made by Hasheminia et al. [11], who studied failure in dis-

*Corresponding author: N. Habibi (Assistant Professor)
E-mail address: n.habibi@uok.ac.ir
10.22084/JRSTAN.2025.31011.1269
ISSN: 2588-2597

Copyright ©2025 The Authors. Published by Bu-Ali Sina University. This work is licensed under a Creative Commons Attribution-NonCommercial 4.0 International license (https://creativecommons.org/licenses/by-nc/4.0/). Non-commercial uses of the work are permitted, provided the original work is properly cited.

similar adherends, and Monteiro et al. [12], who modeled fatigue degradation using cohesive zone models. Fernández et al. [13] and de Moura et al. [14] contributed to delamination and fracture models, and Kim et al. [15] developed failure envelopes for graded joints under mixed-mode loading. Importantly, da Silva et al. [16] introduced magnetic microparticle-based adhesives as a practical graded system. Collectively, these studies underscore the benefits of FGMs in bonded joints.

Experimental methods have been central to validating numerical predictions of joint behavior. Ramezani et al. [17] used DIC to capture strain fields in bi-adhesive joints, while Akhavan-Safar et al. [18] evaluated the fatigue life of composite-steel joints under impact, showing that bi-adhesive techniques improved durability. Probabilistic fatigue predictions were advanced by Lyathakula et al. [19], while stochastic methods were applied by Khan et al. [10] in FGM joints. Ghasemvand et al. [20] studied adhesive defects and creep at elevated temperatures, while Fame et al. [21] analyzed damage tolerance in GFRP double-strap joints, and Carrere et al. [22] investigated the role of pores in adhesive failure initiation. These experimental and environmental studies provide critical validation of modeling approaches and highlight durability challenges in service.

Recent trends emphasize advanced modeling methods and AI integration. Liang et al. [23] combined Gaussian process regression with Kalman filters for fatigue life evaluation, while Wei et al. [24] developed a hybrid experimental-numerical framework using FEA-derived features and Gaussian process regression. Zaheri and Mashayekhi [25] proposed reliability-based optimization of bonded joints, and Panigrahi and Nimje [26] provided design guidelines for FG bonded FRP composites. Numerical advances include Sadeghi et al. [27], who compared XFEM and VCCT for crack prediction, and He [28], who provided early FEA of single-lap joints. Basri et al. [29] explored FEA model updating under built-in stresses, while Jia et al. [30] further confirmed the potential of nano-reinforced FG adhesives. Wei et al. [31] developed a data-driven framework that fuses experimental observations and FEA-derived features—such as substrate thickness, line loads, and bending moments—to train a Gaussian process regression model capable of accurately predicting the fatigue life of automotive adhesive joints across various configurations. Complementing this, Ries [32] provides a comprehensive review of modeling strategies—spanning molecular dynamics, cohesive zone models, and multiscale continuum methods—offering critical guidance on selecting appropriate simulation techniques for adhesive joint performance estimation. Collectively, these studies indicate a shift toward hybrid data-driven and multiscale approaches that enhance predictive accuracy, structural reliability, and design flexibility.

This study introduces a 3D FE framework integrated with AI-based predictive modeling to analyze double-lap adhesive joints with FGM adherends. Unlike prior works limited to 2D or homogeneous models, our approach captures complex stress distributions, optimizes joint design, and improves reliability assessment, offering a significant step forward in evaluating the structural performance of adhesively bonded joints.

2. Mathematical model of FGMs

FG-bonded joints present even greater potential for reducing stress concentrations and the tailoring of stress distribution as desired in an adhesive layer. This capability provides an opportunity for the design of high-performance tailored structural assemblies [33]. In FGMs, the mechanical properties under a given function change continuously in one or more directions. Various mathematical models have been proposed for the variation of these materials' properties. In most cases, a material with graded properties consists of two components: ceramic and metal. Anasiewicz and Kuczmaszewski considered changes in the values of Young's modulus distributed along with the joint thickness [34].

If $\mathrm{V_m}$ and $\mathrm{V_c}$ are considered as the volume of metal and ceramic, respectively, the volume fraction of each material is defined in Formula (1).

$$V_m = \frac{V_m}{V_m + V_c}, \qquad V_c = \frac{V_c}{V_m + V_c} \tag{1}$$

In this relation, V_c and V_m are the volume fractions of ceramic and metal, respectively, in the material with graded properties which follow Equation (2):

$$V_m + V_c = 1 \tag{2}$$

The properties of FG material are as follows:

$$P_{eff} = P_m V_m + P_c V_c \tag{3}$$

Where P_{eff}, P_m and P_c are the effective mechanical properties of the material with graded properties, mechanical properties of metal, and mechanical properties of ceramic, respectively [10].

3. Numerical Method

From the results of previous studies, it is observed that much research on adhesive joints has considered various parameters, such as adhesive type and joint plate type (e.g. homogeneous or composite plates). Composite and FG materials as well as geometric properties of joints, such as single-lap, double-lap, stepped, slopping, and tubular joints, have been used in previous studies.

The results of this research show that the maximum shear stress in the adhesive joint layer occurs at its ends, while the tension in the middle part is very

low and uniform, and the probability of rupture in the corner areas is higher in other areas. However, research on FGM adhesive joints has been very limited, and adhesive bonding in a double-lap arrangement in FGM plates has not yet been conducted. In this research, by applying a tensile force to a double-lap adhesive joint with FGM plates and varying the adhesive thickness, the results are obtained by examining von Mises and shear stresses in the plates and adhesive using both numerical methods and a neural network for comparison . In this research, the proposed joint consists of four plate layers that are glued together . It should be noted that there is no adhesive between the two inner edges of the center plates. Fig.1a shows the connection under consideration. The plates used in this connection are of FGM type, and adhesive is used to bond them.

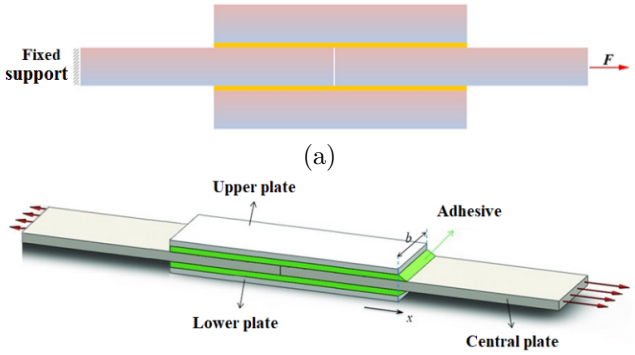

Fig. 1. a) Schematic diagram of the symmetric double-lap adhesive joint with FGM outer adherends and a central metallic inner adherend, b) three-dimensional finite element mesh of the adhesive joint model.

The four plates each have a length of 200mm and are connected to the central plates with an overlap of 100mm, and to the upper and lower plates with an overlap of 200mm utilizing an adhesive with a shear modulus of 1.928GPa. The geometric parameters and properties of the adhesives and plates are provided in Table 1 and Fig. 2a.

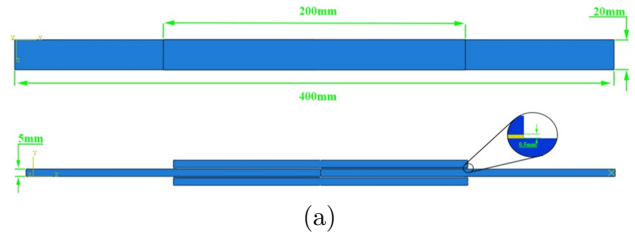

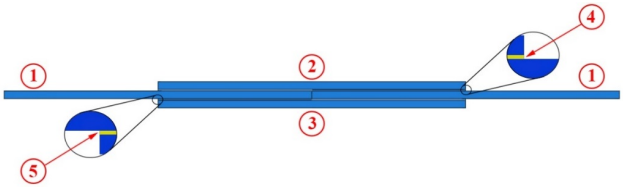

Fig. 2. a) Schematic of double-lap adhesive bonding joint, b) the title of the various parts of the adhesive joint.

The different parts of the connection are defined according to Fig. 2b as follows: 1) Central plate, left and right, 2) Top plate, 3) Bottom plate, 4) Top adhesive, and 5) Bottom adhesive. In this research, the connection used was simulated in 3D with four FGM plates and two adhesive layers as a double-lap joint by applying tensile force using ABAQUS software. UMAT subroutine was used to define the material properties. Finally, after meshing and applying forces and boundary conditions, the desired subroutine was provided to the program as Fortran code, and the simulation results were extracted. Boundary conditions on one side were fully constrained in all directions. The load was also applied as a tensile force in the horizontal direction, along the adhesive bonding direction, with magnitudes of 100kN and 500kN.

3.1. UMAT Subroutine Algorithm

Fig. 3a illustrates the complete FE modeling procedure used to analyze the adhesive stress distribution in a double-lap joint with FGM adherends. The process begins with inputting joint geometry parameters such as adhesive thickness t_a, adherend thickness h, gradient index n, and overlap length L_a. Next, the FGM properties are defined using a power-law distribution for the elastic modulus across the thickness. Adhesive properties-including Young's modulus E_a, Poisson's ratio v, and adhesive thickness t_a-are then assigned. Following this, a computational mesh is generated with refined resolution near the adhesive layer to capture stress concentrations accurately. Loads are applied according to the specified boundary conditions, and the simulation is executed in ABAQUS. Finally, the resulting interfacial shear stress t_{ax} is extracted and analyzed. The flowchart employs standardized shapes and clear stepwise transitions to guide the modeling workflow. To accurately define the growth of the modulus of elasticity of the FG material, the elastic modulus growth contour of the joint is shown in Fig. 3b.

Table 1
Geometric parameters, properties of FGM plates, and the adhesive layer between them [35,36].

Material		Elasticity modulus (GPa)	Poisson's ratio	Length (mm)	Width (mm)	Thickness (mm)
FGM plates	Ni	199.5	0.275	200	20	5
	Al_2O_3	393				
Adhesive	Epoxy	4.82	0.25	200	20	0.05-0.4

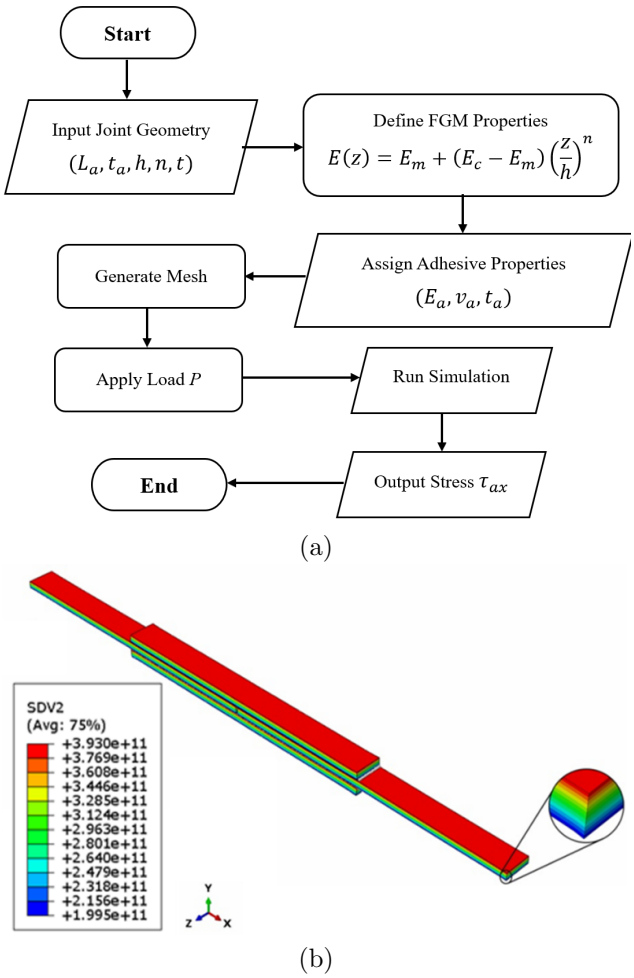

Fig. 3. a) Flowchart of UMAT subroutine algorithm, b) the elastic modulus growth contour of the joint.

3.2. Limitations of the Finite Element Model

While the FEA conducted in this study provides valuable insights into the stress distribution in double-lap adhesive joints with FGM adherends, several limitations must be acknowledged to contextualize the results properly.

First, the model assumes perfect bonding between the adhesive and the adherends, meaning that no interfacial debonding, delamination, or progressive failure mechanisms are considered. In real-world applications, adhesive joints are prone to damage initiation at the interface due to micro-voids, thermal cycling, or manufacturing imperfections-factors that are not captured in the present model.

Second, all materials, including the epoxy adhesive and FGMs, are treated as linear elastic and isotropic, which may oversimplify actual behavior, especially under high loads or long-term service conditions where plasticity, creep, or viscoelasticity could become significant.

Third, the simulation neglects thermal effects, such as residual stresses from curing or temperature gradients, which can significantly influence stress development in adhesive joints. The absence of coupled thermo-mechanical analysis further limits the model's predictive capabilities under varying environmental conditions.

Additionally, the FEA model does not include damage evolution laws or fracture criteria, which are essential for accurately predicting failure locations or modes in joints subjected to complex loading. While the ANN model trained on FEM data captures general stress trends, it inherits these limitations as it relies on idealized inputs.

Lastly, manufacturing-induced defects, such as air entrapment, surface roughness variations, or imperfect adhesive spreading, are not modeled. Such defects can alter stress distributions and reduce bond strength in practical scenarios. Despite these limitations, the FEA framework offers an efficient and informative tool for evaluating joint performance trends and supporting ANN-based predictive modeling. Future work should incorporate damage mechanics, thermal effects, and experimental validation to enhance realism and robustness.

3.3. Contact Definition

In the FE model, the interaction between the adhesive and the adherends was modelled using a surface-to-surface contact formulation to ensure accurate transfer of interfacial stresses. A general contact algorithm was implemented within ABAQUS, with the penalty method selected to enforce the contact constraint. This approach allows a small amount of permissible penetration between contact surfaces, which is corrected by applying restoring forces proportional to the penetration depth. The master surface was assigned to the stiffer FGM adherends, while the adhesive layer was treated as the slave surface to enhance contact stability. Frictionless conditions were assumed, and no separation or sliding was permitted during load application, consistent with the assumption of perfect bonding. This contact configuration ensured numerical convergence and accurately capturing interfacial shear stress development during tensile loading.

3.4. Mesh Generation, and Convergence Behaviour

Mesh generation plays a critical role in accurately capturing the mechanical response of adhesive joints, especially when FGMs are involved. In this study, the mesh was constructed using structured hexahedral (brick) elements, which are well suited for simulating the high stress gradients at interfaces and within the adhesive layer.

To capture the significant variations in material properties across the thickness of the FGM adherends

and accurately model the shear stress distribution in the adhesive layer, a high-density mesh was implemented. The total number of elements in the final model reached approximately 3,200,000. This element count was selected based on a convergence study, in which maximum stress values and stress distribution profiles were monitored as the mesh density increased. It was observed that beyond this mesh size, further refinement led to negligible changes in results (less than 2% variation in peak stress), indicating convergence had been achieved.

Moreover, the use of FG adherends introduces material property gradients, especially in the thickness direction. A coarse mesh would fail to resolve these gradients, leading to errors in stress localization and distribution predictions. To address this, the mesh was refined particularly in:

- The thickness direction of the FGMs, where Young's modulus varies continuously.
- The adhesive layer, where sharp interfacial stress peaks typically occur near the overlap ends.
- The overlap region, where multiaxial stress states dominate due to the interaction of bonded layers.

The dense mesh enables the model to accurately capture stress transfer mechanisms, shear lag effects, and edge stress concentrations without compromising numerical stability. Additionally, the selected mesh ensures consistency with the high-resolution output required for training the ANN model, allowing the extraction of detailed stress patterns across the joint.

In summary, the adoption of a 3,200,000-element mesh is justified by the convergence behavior of the model, the need to resolve fine gradients in material properties and stresses, and the requirement for high-fidelity stress data suitable for ANN integration.

Previous studies have shown that using 320,000 elements to solve problems provides a high rate of convergence. Also in this range, the changes in maximum stress are less. Mesh convergence table based on stress changes and the number of elements illustrated in Table 2.

4. Theoretical Background and Governing Equations

This section presents the essential analytical framework used to support the FE modeling and ANN validation. The formulation includes the stress transfer model for the adhesive layer and the elastic gradation for FGM adherends. Only equations directly related to the configuration studied are retained for clarity and relevance. Fig.4 shows the schematic of a symmetric double-lap adhesive joint, where two FGM outer adherends are bonded to a central metallic adherend using a thin epoxy adhesive layer of thickness t_a. The applied tensile load P is symmetrically distributed, and the joint exhibits plane strain behavior in the overlap region. The adherends are functionally graded in the thickness direction, and the adhesive layer is considered linearly elastic.

Table 2
Mesh convergence is based on stress changes and the number of elements.
(Number of warning elements=0%, Number of error elements=0%)

Number of analyses	Type of element	Total number of elements	Max shear Stress (MPa)
1		5000	22.304
2		20000	25.979
3		80000	27.636
4	C3D8	180000	29.357
5	C3D8R	**320000**	28.425
6		500000	28.433
7		720000	28.448
8		980000	28.431

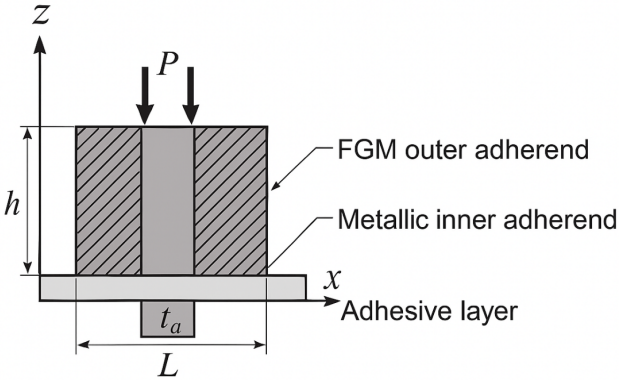

Fig. 4. Geometry and coordinate system for analytical modeling of the joint.

The mechanical properties of FG adherends vary continuously through their thickness based on a power-law distribution:

$$E(z) = E_m + (E_c - E_m)\left(\frac{z}{h}\right)^n \tag{4}$$

$$\rho(z) = \rho_m + (\rho_c - \rho_m)\left(\frac{z}{h}\right)^n \tag{5}$$

where: $E(z)$: Young's modulus at thickness position z; E_m, E_c : Elastic moduli of metal and ceramic phases; $\rho(z)$: Density variation; h : total thickness of the FGM plate; n : gradient index; and $0 \leq z \leq h$. These expressions are implemented in the FEM model using spatially defined fields in ABAQUS.

The shear stress in the adhesive layer under elastic conditions is modeled using a one-dimensional shear-lag formulation:

$$\frac{d^2t(x)}{dx^2} = \frac{2G_a}{t_a}\left(\frac{u_0(x) - u_i(x)}{t_a}\right) \tag{6}$$

$$\tau(x) = \frac{P}{2bt_a}(1 - \frac{x}{L}) \tag{7}$$

where: $\tau(x)$: shear stress distribution along the bond length; G_a : shear modulus of the adhesive; t_a : adhesive thickness; $u_0(x)$: displacement of outer and inner adherends; L : overlap length; and b : width of the joint. This simplified solution is used for validation against FEM-predicted stresses and to generate inputs for ANN training. At the end of the overlap, the maximum shear stress occurs. Assuming a linear elastic adhesive behavior and perfect bonding:

$$t_{max} \approx= \frac{P}{2bt_a} \tag{8}$$

This analytical value is used as a comparative benchmark during mesh validation and ANN output verification.

Results and Discussions

At this stage, numerical results were extracted and analyzed. Analysis was performed for different thicknesses of the adhesive layer, and stress distributions at different distances from the center was extracted. Then, with the help of an ANN, the obtained numerical results were compared with each other, and the best possible case was introduced.

4.1. Central Plates

Figs. 5a shows the areas under stress from the tensile load. The support area withstands a large amount of stress, and approaching the middle joint area will reduce the amount of stress due to the stress distribution of the adhesive and the plates. Examining the central, left, and right plates, Fig. 5b shows a fundamental difference compared to the other plates.

The middle area of the plates in the contact part of the adhesive bears less stress than the size of the components. In the middle region, stress is distributed among the four plate layers and two adhesive layers, resulting in lower stress on the central portions of the two central plates. However, at the ends, parts of the two central plates, due to the reduction of the cross-sectional area, bear all the applied stresses; therefore, the stress increases in the middle of the end of the central plates. And the greatest stress occurres at the end edges of the adhesive and the place of application of force and support of the plates. This can be seen in the diagram shown in Figs. 6a, b.

It is observed that the tension increases with increasing applied force. However, the overall shape of the stress diagram remains almost the same across different loads. The stress applied to the right plate in the direction of 0 and 10mm from the center, the range of 0 to 20mm has an upward trend and will continue with a steep slope in the range of 60 to 100mm. After crossing the ascending range, the stress stabilizes. The chart then goes through a downward trend from 190 to 200mm. In the left plate, due to the symmetry of the graph, the stress trend is in the form of a right plate, which is placed in negative coordinates to be shown in a graph. The main difference between the thicknesses of the adhesive is mostly in the range of 60 to 100mm, corresponding to the region where the adhesive joins the plates. The maximum von Mises stress at forces of 10kN and 50kN belongs to the thickness of 0.05mm of adhesive in the coordinates of 100mm of the diagram, which is related to the area where the end edge of the adhesive joins the middle of the plate. These results are extracted from different paths and can be seen in Figs. 6c, d. From the diagrams, the greater the distance from the center (d), the greater the maximum stress. This is also true for the thickness of the adhesive, and the thicker the adhesive layer, the lower the maximum amount of stress. These results are obtained for various applied forces and adhesive thicknesses.

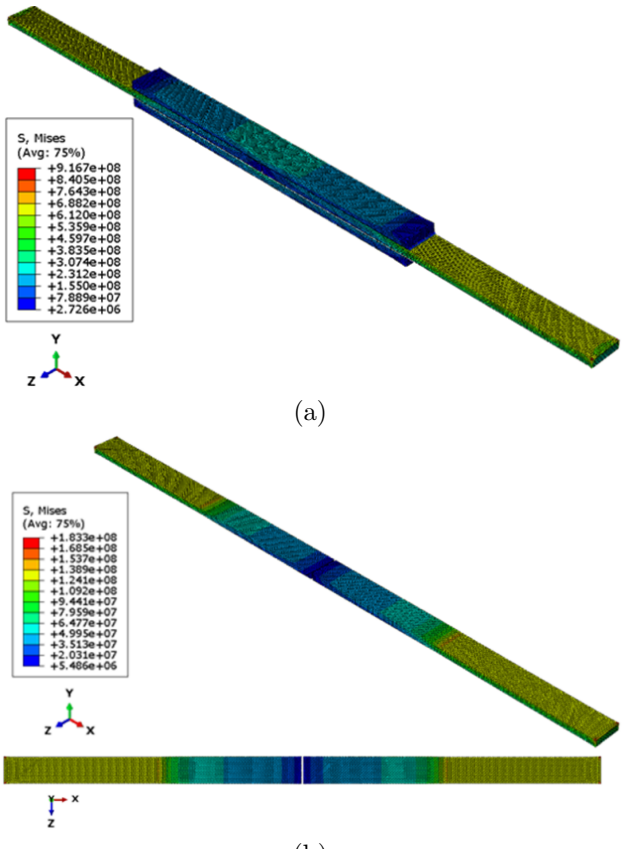

Fig. 5. a) Stress contour in the double-lap adhesive joint with FGM plates (F=50kN), b) the von Mises stress contour in the center plate.

4.2. Upper Plate

All analyses were performed on the middle plane, on the top (upper) and bottom (lower) plates. Thus, the above results were extracted from the center of the top plate for 0.05 to 0.4mm thicknesses of adhesive, 10kN and 50 kN forces, and in 0 to 10mm paths (in 6 different paths).

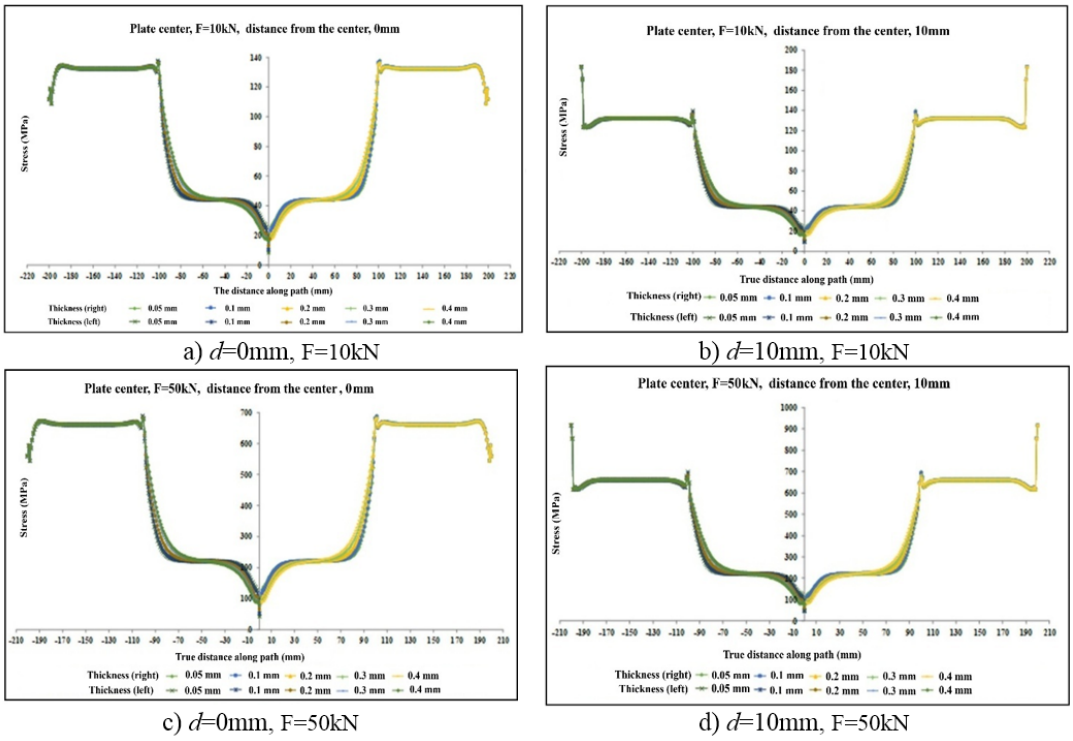

a) d=0mm, F=10kN b) d=10mm, F=10kN

c) d=0mm, F=50kN d) d=10mm, F=50kN

Fig. 6. The von Mises stress contour in the center plates with two distances from the center.

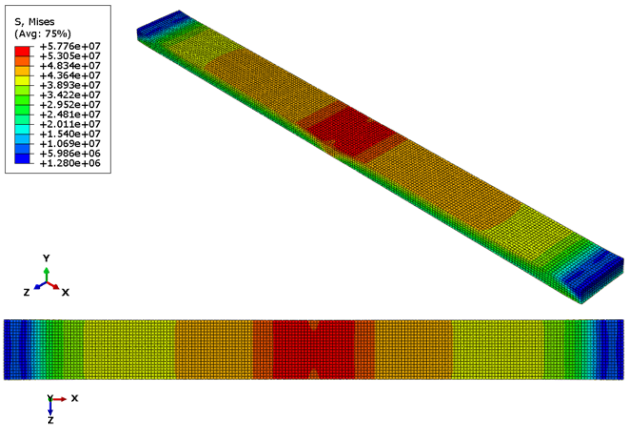

Fig. 7. The von Mises stress contour in the upper plate.

Fig. 7 shows the von Mises stress contour of the top plate. According to the contour of Fig. 7, the stress in the middle of the plate has a maximum value and by moving to the sides, the amount of stress is reduced. The maximum stress at 10kN is 57MPa. It should be noted that due to the lack of an adhesive layer in the head-to-head connection of the two middle plates, critical stress occurs in the middle of the two upper and lower plates. As was done to analyze the stress distribution of the middle plate, diagrams were extracted to distribute the stress on the upper plate. In Figs. 8a, b, and Figs.8c, d, in the paths 0 and 10mm from the center (path passing through the center) approaching the center in the range of 70 to 130mm, there is an increase in stress. Also, there is a relative drop in the middle part of the plate due to the discontinuity in the connection between the two middle plates.

It can also be seen that as the thickness of the adhesive layer increases, the stress on the sides of the upper plate decreases, and these are the opposite for areas close to the center. The maximum stress of von Mises occurs in the thickness of 0.4 mm of the adhesive layer and the coordinates of 95- and 105 mm. Comparisons show that with increasing distance from the center, the maximum stress increases.

4.3. Lower Plate

Similar to the upper plate, the stress distribution for different adhesive thicknesses was investigated on the lower plate. The results were obtained for applied loads of 10kN and 50kN. Figs. 9a-d, show the von Mises stress distribution for 0mm and 10mm paths from the center for forces of 10kN and 50kN. As can be seen from the diagrams, stress in the lower plate exhibits a steep upward trend in the initial 10mm and a steep downward trend in the final 10mm, symmetrically. In the range of 10 to 90mm and 110 to 190mm, the stress trend is relatively steady. However, in the middle region (90–110mm), stress peaks sharply, reaching a maximum of 86.572 MPa at 10kN and 464.864MPa at 50kN for an adhesive thickness of 0.05mm, located at the center between the two plates. It should be noted that increasing the adhesive thickness reduces the stresses on the plate. Comparisons showed that the maximum stress increases with increasing distance from the center.

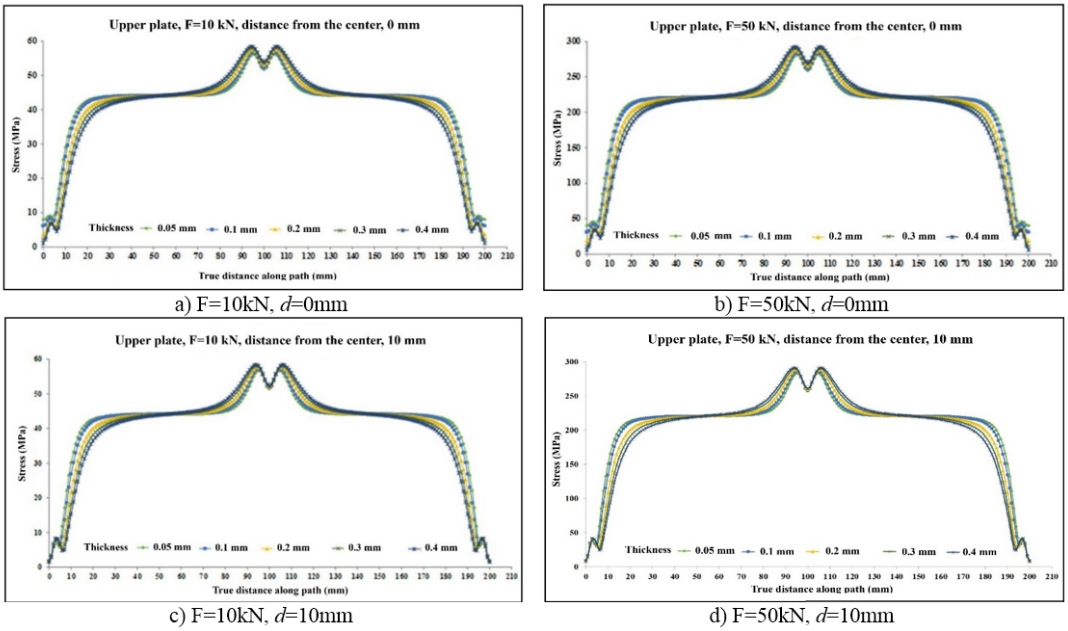

a) F=10kN, d=0mm b) F=50kN, d=0mm

c) F=10kN, d=10mm d) F=50kN, d=10mm

Fig. 8. The von Mises stress contour in the upper plates with two distances from the center.

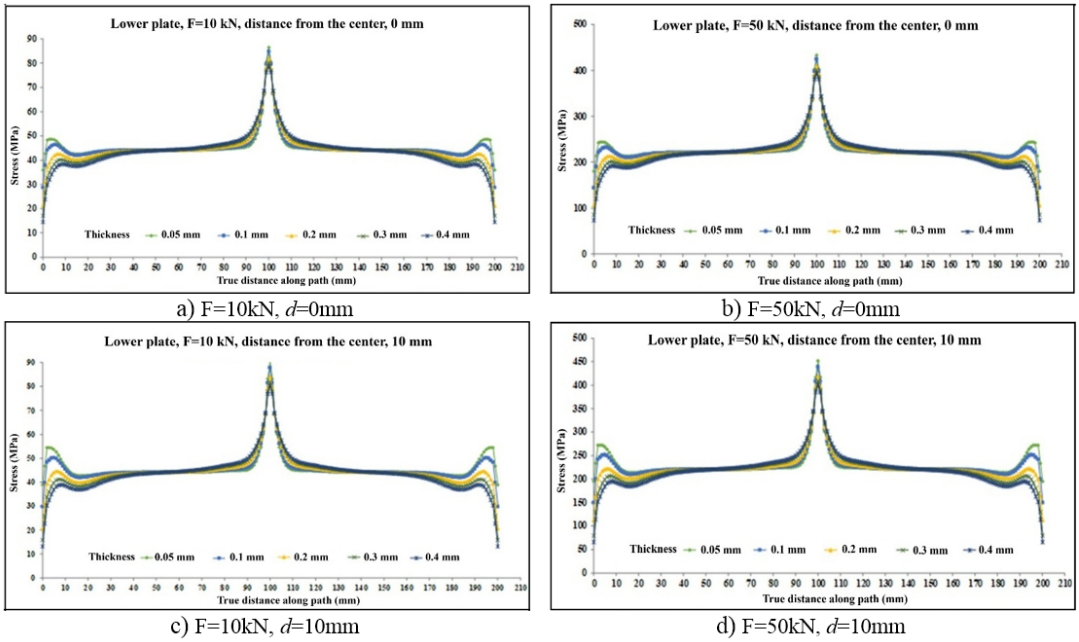

a) F=10kN, d=0mm b) F=50kN, d=0mm

c) F=10kN, d=10mm d) F=50kN, d=10mm

Fig. 9. The von Mises stress contour in the lower plates with two distances from the center.

4.4. Adhesive Layers

Figs. 10a and 10b show the von Mises stress distribution in the upper and lower layers of adhesive. The study of the stress contour of the upper adhesive layer can be discussed in two separate parts. On the right side of the loading site, the maximum stress of 18MPa at a force of 10kN is applied to the adhesive. Stress transfer from the upper plate to the upper adhesive causes a sudden increase in stress in the middle of the adhesive near the end of the right half. In the middle region of the adhesive, in the initial half and the left half, the amount of stress is reduced, which is due to the transfer of stress to the central support plate. The opposite trends is observed in the lower adhesive layer.

Considering the change of maximum shear stresses at different thicknesses of adhesive and the use of standard paths for extracting shear stress and Von-Mises stress diagrams, tracking maximum shear stress points across different adhesive thicknesses indicate that the maximum shear stress is 0.2mm thick. At this thickness, the adhesive reaches its optimal stress state, as shown in Figs. 11a and 11b.

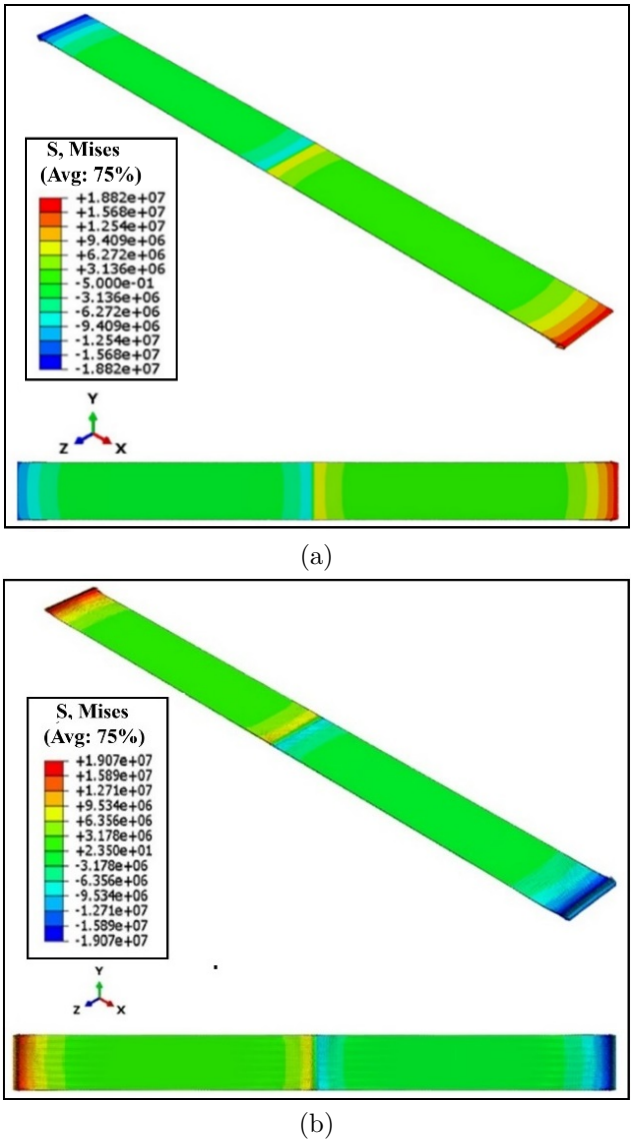

Fig. 10. The von Mises stress contour in the layers of adhesive.

4.5. Asymmetrical Stress Distribution and Bending Behavior

The stress distribution in double-lap adhesive joints is significantly influenced by the relative stiffness and geometry of the adherends. Although the joint is geometrically symmetric, the outer adherends-made of FGMs-exhibit a graded variation in their elastic modulus that introduces a mechanical asymmetry in their response to loading.

Specifically, the modulus of elasticity in each FGM adherend varies nonlinearly through its thickness, following a power-law distribution. This gradation results in different bending responses in the upper and lower plates. Under tensile load, the upper plate, which is typically adjacent to a stiffer (ceramic-rich) region, demonstrates reduced bending and higher resistance to deformation. In contrast, the lower plate, being closer to the more ductile (metal-rich) zone, undergoes greater curvature. This difference produces a non-uniform distribution of interfacial stresses in the adhesive layer.

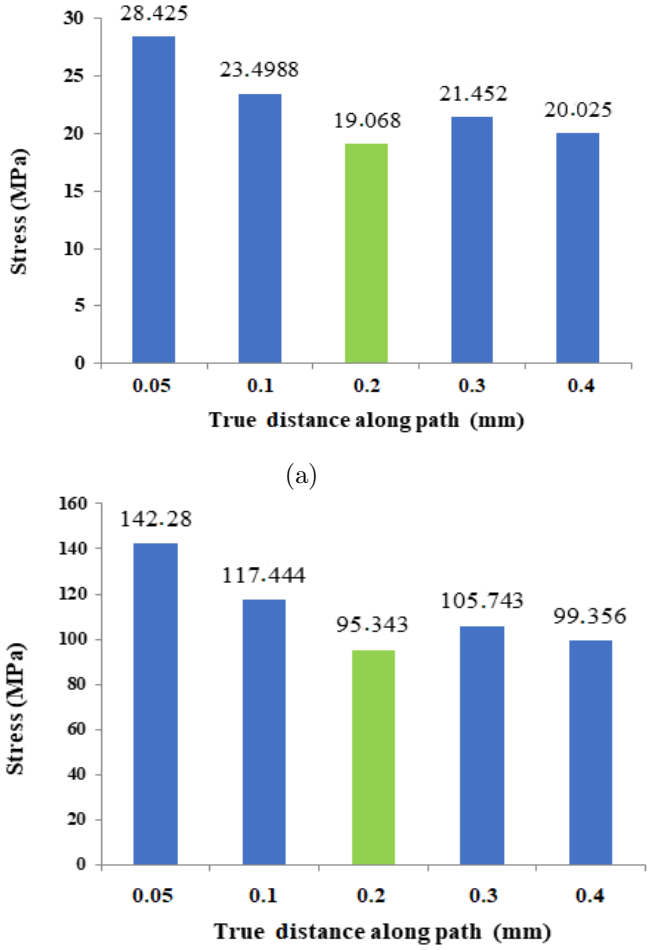

Fig. 11. Maximum stress values in terms of adhesive thickness.

The asymmetry in stress distribution, as shown in these figures, is attributed to the differential bending stiffness caused by the graded material properties. In the upper plate, the higher stiffness reduces deflection, resulting in more uniform load transfer along the adhesive bond line. Conversely, the enhanced bending of the lower plate leads to concentrated stress regions, particularly near the free edges of the adhesive joint. These observations emphasize that even in symmetric joint configurations, gradation in adherend properties induces bending differences that critically affect adhesive performance. integration of these findings into our ANN model further validates the approach, as the network successfully predicts the observed trends by implicitly accounting for the effects of modulus gradation and bending.

4.6. Validation of Results

To validate the numerical results of this study, the model reported in [37] was simulated using ABAQUS software to extract the shear stress diagram of the adhesive at the edge of a joint. The reference model is shown in Fig. 12a. In the present study, the same model was analyzed in ABAQUS software, and the results were compared. Fig. 12b clearly shows that the process of this study is accurate. In this paper, two different configurations were considered using the model to examine the effects of varying the modulus of elasticity in FGM plates at the edge of a joint . In the first configuration, the FG materials of the adhesives (plates) are arranged in such a way that their axial stiffness varied from 199.5GPa in contact with the adhesive to 393.39GPa at the free surface (Fig. 12c). In the second configuration, the adhesives (plates) are arranged in such a way that their axial stiffness varies from 393GPa in contact with the adhesive to 199.5GPa at the free surface (Fig. 12d). The results of this study show that the intensity of shear stress is significantly reduced near the free edges of the adhesive (corners) in the configuration where the stiffener is placed at the free surface.

4.7. Artificial Neural Network Architecture and Implementation

To complement the finite element simulations and enable rapid prediction of stress responses in double-lap adhesive joints, an ANN model was developed using data generated from ABAQUS simulations. The ANN was trained to predict the maximum shear stress in the adhesive layer based on key input parameters: adhesive thickness, material gradation index, and applied tensile load. The ANN model follows a feedforward architecture consisting of:

Three input neurons, corresponding to adhesive thickness (mm), gradation index (n), and applied load (N);

One hidden layer with seven neurons, determined through trial-and-error and convergence testing to balance accuracy and overfitting risk;

One output neuron, representing the predicted maximum shear stress (MPa).

The sigmoid (log-sigmoid) activation function was used in the hidden layer to introduce nonlinearity and ensure smooth gradient flow. The output neuron employed a pure linear activation function, suitable for regression-type predictions. The model was trained using the Levenberg–Marquardt backpropagation algorithm, chosen for its fast convergence and accuracy in function approximation problems. To ensure generalization, the dataset was randomly divided as: 70% for training, 15% for validation, and 15% for testing.

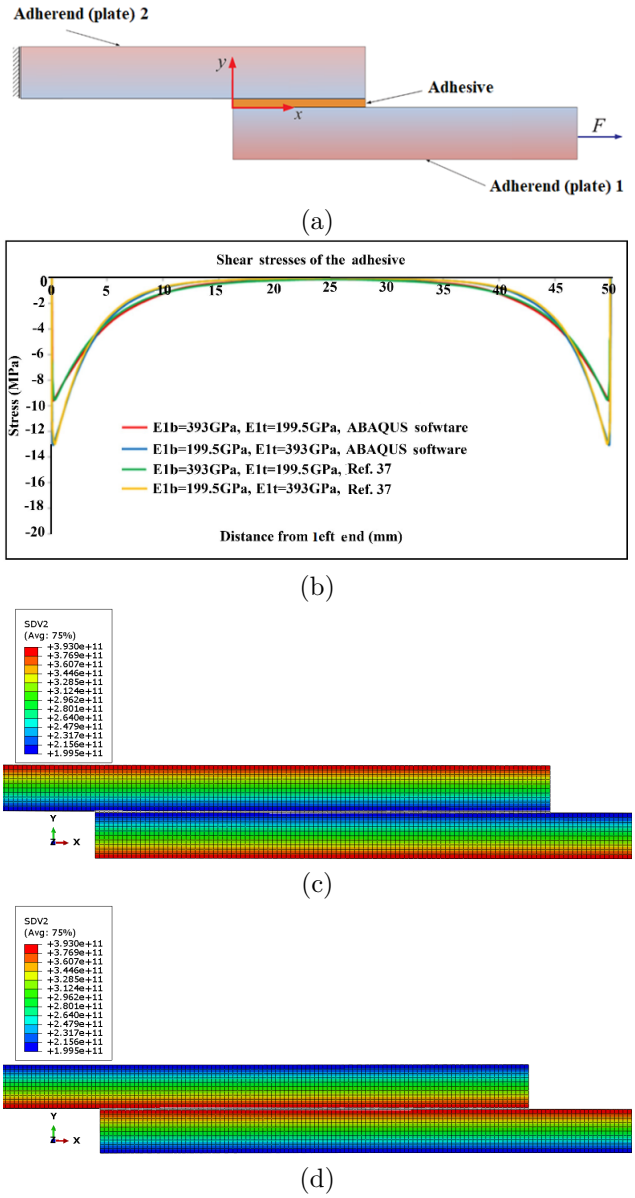

Fig. 12. a) The model is studied in Ref [19], b) shear stress diagram along with the adhesive layer for two FGM plate configurations, c) First configuration of the connection, d) Second Configuration of the connection.

The input dataset comprised simulation results from 60 different combinations of adhesive thicknesses (0.1–0.5mm), material gradation indices (n=1 to 10), and applied loads (10kN and 50kN). The performance of the trained ANN was evaluated using the mean squared error (MSE) and correlation coefficient (R^2) between predicted and FEM-derived values. The model achieved an MSE below 0.001 and an R^2 greater than 0.99, confirming high prediction accuracy. This ANN framework enables rapid stress estimation in similar joint configurations and can serve as a surrogate model in optimization workflows or parametric sensitivity studies. The following assumptions are considered in modeling the ANN.

- Information processing is done in simple and numerous elements called neurons.
- The signal is transmitted between neurons through the connection between them.
- Each connection has its weight, which is multiplied by the transmitted signal.
- The output signal of the neuron is obtained by applying the excitation function (usually nonlinear) to the weighted sum of the input signals.
- Neuro-solution software is useful for implementing problem-solving with the help of a neural network.

In this study, a multilayer perceptron neural network with three inputs was used to determine the optimal network. To develop the neural network models, the data was first divided into three subsets: 70% for training, 10% for validation, and the remaining 20% for network testing. The network was validated after each training iteration . After the training and validation steps, the network was tested for data that has not been employed before. The model of this network is shown in Fig. 13a.

Table 3
Training and validation results of the neural network model.

Raw	Structure	Minimum MSE	Correlation coefficient	Accuracy of forecasting
1	3-3-1	0.0187	0.83	70.01
2	3-4-1	0.0093	0.78	41.38
3	3-5-1	0.0087	0.91	84.64
4	3-6-1	0.0099	0.89	93.13
5	**3-7-1**	**0.0065**	**0.96**	**97.13**
6	3-8-1	0.0081	0.90	91.06
7	3-9-1	0.0083	0.89	95.72
8	3-10-1	0.0091	0.93	93.14

Table 3 shows the results of the neural network model with different number of hidden layers. The greater the number of hidden layers, the more training iterations are needed for the network to adapt , and as the number of these layers increases to a certain extent, the error in network training decreases to a greater extent. In neural networks, rapid network adaptation is of particular importance. Although the speed increases as the number of hidden layers decreases, the errors will increase to some extent. To select the appropriate network after the test, a network of acceptable errors and higher speed must be selected. The results of the neural network model, compared with the ABAQUS simulation for maximum shear stress relative to adhesive thickness at loads of 10kN and 50kN (Figs. 13b, c), show a high degree of agreement. It should be noted that the maximum shear stress with a rate of 94.34MPa corresponds to a thickness of 0.2mm, which in this regard is consistent with the output data of ABAQUS software. Results of the neural network model test to determine the adhesive shear stress at thicknesses increments of 0.01mm are shown in Table 4.

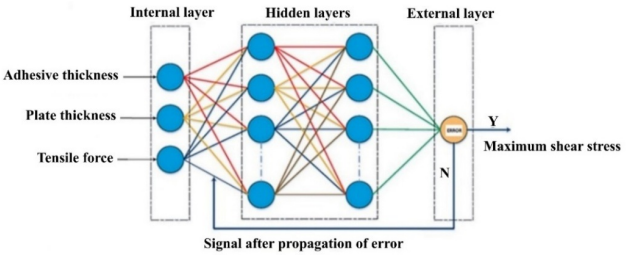

(a)

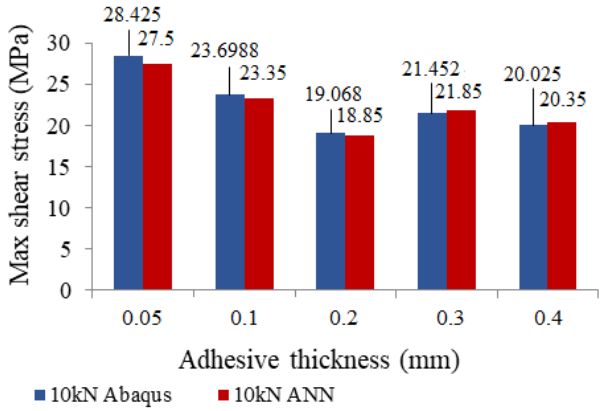

(b)

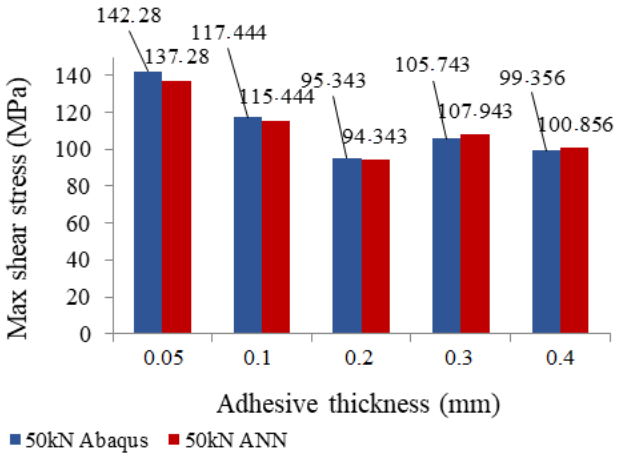

(c)

Fig. 13. a) Perceptron neural network model, b) , c) Comparison of artificial neural network results and ABAQUS simulation results for maximum shear stress relative to the adhesive thickness.

5. Conclusions

The outcomes of this study are presented in several focused sections. In the analysis of stress distribution along the left and right centre plates, it was observed that the cross-sectional area at the extreme

edges (±100mm) corresponds to that of a single central plate. However, within the central 200mm of the overlap region, the effective cross-sectional area increases due to the interaction of all three plates bonded via the adhesive layer. Consequently, the central section of the joint exhibits reduced stress in the centre plate compared to the end regions.

Table 4
Results of the ANN model test to determine the adhesive shear stress at thicknesses increments of 0.01mm.

Adhesive thickness	F=10kN		F=50kN	
(mm)	ABAQUS	ANN	ABAQUS	ANN
0.05	28.42	25.50	142.28	137.28
0.06		25.14		132.67
0.07		24.89		128.45
0.08		24.56		122.05
0.09		23.95		117.85
0.10	23.69	23.35	117.4	114.27
0.12		22.62		113.16
0.13		22.34		112.25
0.14		21.92		110.22
0.15		21.56		108.65
0.16		20.74		105.95
0.17		20.16		104.12
0.18		**18.56**		101.19
0.19		19.23		97.63
0.20	19.068	18.85	95.452	94.34
0.21		18.96		**94.26**
0.22		19.07		94.78
0.23		19.25		95.83
0.24		19.74		97.47
0.25		20.11		98.14
0.26		19.84		101.36
0.27		20.33		99.71
0.28		20.76		103.29
0.29		21.28		105.53
0.30	21.45	21.85	105.74	107.94
0.31		21.62		106.25
0.32		21.79		106.79
0.33		21.54		104.37
0.34		21.36		104.08
0.35		21.41		103.65
0.36		21.30		103.17
0.37		20.97		102.59
0.38		20.59		101.59
0.39		20.42		101.36
0.40	20.025	20.35	99.35	100.85

Due to the discontinuity at the edges of the centre plate, the stress distribution becomes non-uniform. A sharp reduction in cross-sectional area in the midspan of the joint causes localized stress concentrations in the upper plate. As the stress flow through the central plate is interrupted, load redistribution occurs, transferring the stress path from the centre plate to the adjacent upper and lower plates. This redistribution results in a significant stress increase in the mid-region of the upper plate. Notably, a localized drop in stress is observed approximately 10mm from the centreline, attributed to stress flow disruption and redirection between the bonded layers.

In contrast, stress analysis of the lower plate reveals a different trend. Unlike the upper plate, no stress discontinuity is observed in the middle of the lower plate. This disparity may be attributed to the bending deformation induced during tensile loading, along with the asymmetric variation in the Young's modulus gradient between the top and bottom adherends.

With regard to the adhesive layer, the upper surface exhibits an increasing stress trend from the start to the end of the joint, while the lower surface shows a decreasing trend. This opposite behaviour is due to the shift in loading mode from tensile to compressive forces along the bond line. The resulting stress flow in the upper and lower adhesive layers is therefore reversed. Additionally, shear stress analysis across different adhesive thicknesses indicates that increasing the adhesive layer thickness reduces stress concentrations at the corners and promotes a more uniform stress distribution near the bond centre. The shear stress tends to decrease in the central 20mm of the adhesive due to enhanced load distribution at greater thicknesses.

An ANN model was developed to further interpret the results. The network demonstrated excellent accuracy in predicting stress behaviour, closely matching the outcomes of the finite element simulations and validating its capability as a robust predictive tool.

References

[1] L. D. C Ramalho, R. D. S. G. Campilho, J. Belinha, L. F. M. da Silva, Static strength prediction of adhesive joints: a review, Int. J. Adhes. Adhes., 96 (2020) 102451.

[2] A. Akhavan-Safar, F. Ramezani, F. Delzendehrooy, M. R. Ayatollahi, L. F. M. da Silva, A review on bi-adhesive joints: benefits and challenges, Int. J. Adhes. Adhes., 114 (2022) 103098.

[3] J .F. Durodola, Functionally graded adhesive joints-A review and prospects, Int. J. Adhes. Adhes., 76 (2017) 83-100.

[4] L. F. M. da Silva, P. J. C. das Neves, R. D. Adams, A. Wang, J. K. Spelt, Analytical models of adhesively bonded joints-Part I: literature survey, Int. J. Adhes. Adhes., 29(3) (2009) 319-330.

[5] L. F. M. da Silva, P. J. C. das Neves, R. D. Adams, A. Wang, J. K. Spelt, Analytical models of adhesively bonded joints-Part II: comparative study, Int. J. Adhes. Adhes., 29(3) (2009) 331-341.

[6] R. J. C. Carbas, L. F. M. da Silva, G. W. Critchlow, M. A. V. Figueiredo, Effect of adhesive type and thickness on the lap shear strength, J. Adhes, 82(11) (2006) 1091-1115.

[7] I. L. Pires, M. F. S. F. de Moura, R. D. S. G. Campilho, Performance of bi-adhesive bonded aluminium lap joints, Int. J. Adhes. Adhes., 23(3) (2003) 215-223.

[8] S. K. Kong, Y. K. Jo, T. H. Kim, J. W. Kim, Three-dimensional finite element analysis of the stress distribution in bi-adhesive bonded joints, J. Adhes., 84(2) (2008) 105-126.

[9] Z. Jia, J. Yu, Q. Liu, S. Yu, Z. Wang, functionally graded adhesive joints with exceptional strength and toughness by graphene nanoplatelets reinforced epoxy adhesives, Int. J. Adhes. Adhes., 125 (2023) 103402.

[10] M. A. Khan, R. Tipireddy, B. Dattaguru, S. Kumar, Stochastic modeling of functionally graded double-lap adhesive joints, Mech. Mate, 177 (2023) 104553.

[11] S. M. Hasheminia, B. C. Park, H. J. Chun, J. C. Park, H. S. Chang, Failure mechanism of bonded joints with similar and dissimilar material, Compos Part B Eng., 161 (2019) 702-709.

[12] J. Monteiro, A. Akhavan-Safar, R. Carbas, E. Marques, R. Goyal, M. El-Zein, L. Da Silva, F Mode II modeling of adhesive materials degraded by fatigue loading using cohesive zone elements, Theor. Appl. Fract. Mech., 103 (2019)102253.

[13] M. V. Fernández, M .F. S. F. de Moura, L. F. M. da Silva, A. T. Marques, Composite delamination rate simulation, Materials (Basel), 12(1) (2019) 181.

[14] M. F. S. F. de Moura, R. D. S. G. Campilho, J. J. L. Morais, Development of a cohesive zone model for fatigue/fracture characterization of composite bonded joints under Mode II loading, Int. J. Adhes. Adhes., 54 (2014) 224-230.

[15] M. H. Kim, H. S. Hong, Y. C. Kim, Determination of failure envelope of functionally graded adhesive-bonded joints by using mixed-mode continuum damage model and response surface method, Int. J. Adhes. Adhes., 106 (2021) 102815.

[16] C. I. da Silva, M. R. O. Cunha, A. Q. Barbosa, R. J. C. Carbas, E. A. S. Marques, L. F. M. da Silva, functionally graded adhesive joints using magnetic microparticles with a polyurethane adhesive, J. Adv. Join. Process., 3 (2021) 100048.

[17] F. Ramezani, M. R. Ayatollahi, L. F. M. da Silva, F. Berto, A comprehensive experimental study on bi-adhesive single-lap joints using DIC technique, Int. J. Adhes. Adhes., 102 (2020) 102674.

[18] A. Akhavan-Safar, F. Ramezani, F. Delzendehrooy, M. R. Ayatollahi, L. F. M. da Silva, Impact fatigue life of adhesively bonded compositesteel joints enhanced with the bi-adhesive technique, Materials (Basel), 16(3) (2023) 6468.

[19] K.R. Lyathakula, Y. Wei, Z. Huang, W. Sun, A probabilistic fatigue life prediction for adhesively bonded joints, Thin Walled Struct., 164 (2021) 107863.

[20] M. Ghasemvand, B. Behjat, S. Ebrahimi, Experimental investigation of the effects of adhesive defects on the strength and creep behavior of single-lap adhesive joints at various temperatures, J Adhes., 99 (2023) 12271243.

[21] C. Fame, J. Ramôa Correia, E. Ghafoori, C. Wu, Damage tolerance of adhesively bonded pultruded GFRP double-strap joints, Compos. Struct., 263 (2021) 113625.

[22] N. Carrere, A. Doitrand, E. Martin, D. Leguillon, Influence of small pores on crack initiation in adhesively bonded joints: a theoretical study. International Journal of Adhesion and Adhesives, 111 (2021) 102979.

[23] T. Liang, Q. He, X. Chen, Gaussian process flow and physical model fusion driven fatigue evaluation model using Kalman filter, Proc. Inst. Mech. Eng. C J. Mech. Eng Sci., 236(21) (2022) 11054-11067.

[24] Y. Wei, W. Sun, Z. Huang, K. R. Lyathakula, Data-driven fatigue life prediction of automotive adhesive joints using Gaussian process regression with FEA-derived features, Finite Elem. Anal. Des., 233 (2024) 104225.

[25] F. Zaheri, M. Mashayekhi, Reliability-based design optimization for adhesive bonded joints, Adv. Mech. Eng., 16 (2024) 168781402495345.

[26] S. K. Panigrahi, S. K. Nimje, Design and analysis of functionally graded adhesively bonded joints of FRP composites, Boca Raton: CRC Press; (2023).

[27] M. Sadeghi, N. Carrere, D. Leguillon, A. Doitrand, E. Martin, Extended Finite Element Method (XFEM) and VCCT for adhesive crack predictions: a comparative study, Materials, 18(15) (2023) 3557.

[28] X.C. He, Finite Element Analysis of Adhesively Bonded Single-lap Joints, Adv. Mater. Res., 129 (2010) 411-415.

[29] A. B. A. Basri, D. W. Chae, H. Lee, Finite Element Model Updating of Composite with Adhesive Jointed Structure Under Built-up Internal Stress, J. Vibration Control, 28(1112) (2022) 21912207.

[30] Z. Jia, J. Yu, Q. Liu, S. Yu, Z. Wang, functionally graded adhesive joints with exceptional strength and toughness by graphene nanoplatelets reinforced epoxy adhesives, Int. J. Adhes. Adhes., 125 (2023) 103402.

[31] C. D. Wei, Q. R. Chen, M. Chen, L. Huang, Z.J. Yue, S.G. Li, J. Wang, L. Chen, C. Tong, Q. Liu. Predicting fatigue life of automotive adhesive bonded joints: A data-driven approach using combined experimental and numerical datasets, Adv. Manuf., 12 (2024) 522537.

[32] M. Ries/ Mechanical behavior of adhesive joints: A review on modeling techniques, Comput. Methods Mater. Sci., 24(4) (2024) 535.

[33] J.B. Marques, A.Q. Barbosa, K. Houjou, C.I. Da Silva, A.J.C. Carbas, L.F.M. Da Silva. An overview of manufacturing functionally graded adhesives- Challenges and prospects, The Journal of Adhesion, 97(2) (2021) 172-206.

[34] K. Anasiewicz, J. Kuczmaszewski, Apparent Youngs modulus of the adhesive in numerical modeling of adhesive Joints, Materials, 14(328) (2021) 1-11. https://doi.org/10.3390/ma14020328

[35] Z. Wang, J. Li, L. Sui, G. Xian, Effects of adhesive property and thickness on the bond performance between carbon fiber reinforced polymer laminate and steel. Thin-Walled Struct., 158 (2021) 107176.

[36] A. Sajjadi, H. R. Ezatpour, H. Beygi, Microstructure and mechanical properties of AlAlO micro- and nano-composites fabricated by stir casting Mater. Sci. Eng. A, 528(24-25) (2011) 8765-8771. doi:10.1016/j.msea.2011.08.052

[37] N. Stein, .PL. Rosendahl, W. Becker, Homogenization of mechanical and thermal stresses in functionally graded adhesive joints, Composites Part B: Engineering, 111 (2017) 279-293. https://doi.org/10.1016/j.compositesb.2016.11.061